Inkjet Printed Circuits with 2D Semiconductor Inks for High-Performance Electronics

Tian Carey,* Adrees Arbab, Luca Anzi, Helen Bristow, Fei Hui, Sivasambu Bohm, Gwenhivir Wyatt-Moon, Andrew Flewitt, Andrew Wadsworth, Nicola Gasparini, Jong M. Kim, Mario Lanza, Iain McCulloch, Roman Sordan,* and Felice Torrisi*

Air-stable semiconducting inks suitable for complementary logic are key to create low-power printed integrated circuits (ICs). High-performance printable electronic inks with 2D materials have the potential to enable the next generation of high performance low-cost printed digital electronics. Here, the authors demonstrate air-stable, low voltage (<5 V) operation of inkjet-printed n-type molybdenum disulfide (MoS_2), and p-type indacenodithiophene-*co*-benzothiadiazole (IDT-BT) field-effect transistors (FETs), estimating an average switching time of $\tau_{MoS2} \approx 4.1$ μs for the MoS_2 FETs. They achieve this by engineering high-quality MoS_2 and air-stable IDT-BT inks suitable for inkjet-printing complementary pairs of n-type MoS_2 and p-type IDT-BT FETs. They then integrate MoS_2 and IDT-BT FETs to realize inkjet-printed complementary logic inverters with a voltage gain $|A_v| \approx 4$ when in resistive load configuration and $|A_v| \approx 1.4$ in complementary configuration. These results represent a key enabling step towards ubiquitous long-term stable, low-cost printed digital ICs.

1. Introduction

Digital integrated circuits (ICs) mainly rely on a metal-oxide-semiconductor (MOS) technology that uses p-type (PMOS logic) or n-type (NMOS logic) field-effect transistors (FETs) to implement mixed signal ICs[1] and logic gates.[2] A complementary MOS (CMOS) logic uses both p-type and n-type FETs and enables ICs with drastically smaller power dissipation than that of PMOS and NMOS logic.[3] Roughly 95% of all modern ICs use CMOS logic,[4] making it a fundamental technology towards low-power, scalable circuits.[4] Figures of merit such as field effect mobility (μ), on/off current ratio (I_{on}/I_{off}), switching time (τ), and inverter voltage gain ($|A_v|$), defined as the slope of the inverter voltage transfer characteristic (dV_{OUT}/dV_{IN}, where V_{IN}

Dr. T. Carey, A. Arbab, Dr. S. Bohm, Dr. F. Torrisi
Cambridge Graphene Centre
Department of Engineering
University of Cambridge
Cambridge CB3 0FA, UK
E-mail: tian.carey@cantab.net; f.torrisi@imperial.ac.uk
Dr. T. Carey, A. Arbab, H. Bristow, Dr. S. Bohm, Dr. A. Wadsworth,
Dr. N. Gasparini, Dr. F. Torrisi
Department of Chemistry
Molecular Sciences Research Hub
Imperial College London
White City Campus, Wood Lane, London W12 0BZ, UK
Dr. L. Anzi, Prof. R. Sordan
L-NESS
Department of Physics
Politecnico di Milano
Via Anzani 42, Como 22100, Italy
E-mail: roman.sordan@polimi.it

Dr. F. Hui
Department of Materials Science and Engineering
Technion – Israel Institute of Technology
Haifa 3200003, Israel
Dr. G. Wyatt-Moon, Prof. A. Flewitt, Prof. J. M. Kim
CAPE Building
Department of Engineering
University of Cambridge
Cambridge CB3 0FA, UK
Prof. M. Lanza
Physical Sciences and Engineering Division
King Abdullah University of Science and Technology (KAUST)
Thuwal 23955–6900, Saudi Arabia
Prof. I. McCulloch
KAUST Solar Center (KSC)
King Abdullah University of Science and Technology (KAUST)
Thuwal 23955-6900, Saudi Arabia
Prof. I. McCulloch
Department of Chemistry
Chemistry Research Laboratory
University of Oxford
Oxford OX1 3TA, UK

is the input and V_{OUT} the output voltage), have been used to assess and benchmark the performance of the FETs and ICs, respectively. Ultra-large-scale integration circuits such as memories, microcontrollers and large-area flexible active-matrix displays rely on CMOS and resistive load (i.e., PMOS and NMOS) logic circuits requiring $|A_v| > 1$, which are achievable in ambient conditions without the use of high-vacuum (< 10^{-6} mbar) technologies.[5]

Printing electronic circuits have the potential to enable low-cost ubiquitous IC systems on arbitrary substrates for flexible[6] and wearable electronics.[7] The key for creating high-performance printed FETs is to ideally obtain a highly crystalline semiconductor channel,[8,9] improve printing uniformity (i.e., decrease the active channel roughness),[9] and remove residual surfactants and solvents from the printed films.[10] Furthermore, optimal printed CMOS logic circuits with $|A_v| > 1$ require reducing the FET threshold voltage, $V_{th} < 1$ V to reduce the power supply voltage and the same drain current I_D levels for both p-type and n-type FETs.[11] Printable electronic inks achieving such performances with conducting, semiconducting, and insulating or dielectric properties is key to satisfy the diverse nature of IC components, such as interconnects, resistors, diodes, capacitors, and transistors.[12,13] Inkjet printing is a prime technique for large-area fabrication of printed electronics, combining advantages such as versatility to print on wide range of substrates (e.g., textile, polymers and silicon), mask-less and non-contact fabrication with a high resolution ($\approx$ 50 μm), manufacturing scalability (m^2 min^{-1}) and low material losses (<1 ml),[7] which make it a well-established technique to print ICs based on PMOS, NMOS, and CMOS technologies.[14]

The majority of scientific efforts towards inkjet printed FETs and CMOS logic is focused on the development of organic polymers, metal oxides, and sorted single walled carbon nanotubes (SWCNTs) as the channel material.[15–17] For example, poly(3-hexylthiophene) (P3HT) has been used as a p-type channel material with an n-type material poly{[N,N9-bis(2-octyldodecyl)-naphthalene-1,4,5,8-bis(dicarboximide)-2,6-diyl]-alt-5,59-(2,29-bithiophene)} (P(NDI2OD-T2)) to enable an organic polymer inkjet printed CMOS inverter on polyethylene terephthalate (PET). The FETs had $\mu < 1$ cm^2 V^{-1} s^{-1}, $I_{on}/I_{off} \approx 10^6$, and $|A_v| \approx 25$.[15] However, organic polymers frequently suffer from long-term (>100 h) stability issues in an ambient condition[18] and n-type organic polymers have struggled to exceed $\mu \approx 1$ cm^2 V^{-1} s^{-1} after decades of research.[19] Doped SWCNTs have been used to achieve inkjet printed FETs with $\mu \approx 2$ cm^2 V^{-1} s^{-1}, $I_{on}/I_{off} \approx 10^5$, and CMOS inverters with $|A_v| \approx 85$ on a Si/SiO$_2$ substrate.[16] Inkjet printed doped metal oxides have also been investigated. Inkjet printed zinc tin oxide was used as an n-type material ($\mu \approx 4$ cm^2 V^{-1} s^{-1}, $I_{on}/I_{off} \approx 10^6$) with inkjet printed p-type SWCNT ($\mu \approx 2$ cm^2 V^{-1} s^{-1}, $I_{on}/I_{off} \approx 10^4$) to enable a CMOS inverter with $|A_v| \approx 17.1$.[17] Unfortunately, SWCNTs require semiconducting versus metallic sorting before deposition, limiting manufacturability.[16]

Electronic few-layer 2D material inks (E2D inks) offer properties suitable to inkjet print ICs.[20] Dispersions of 2D materials can be mass-produced by liquid-phase exfoliation (LPE) and formulated into electronic few-layer E2D inks,[20] with conducting (e.g., MXenes), semiconducting (e.g., transition metal dichalcogenides), and insulating properties (e.g., hexagonal

boron nitride, h-BN, or silicates) suitable for printed and conformable electronics on-demand and in scale.[21] For example, semiconducting molybdenum disulfide (MoS$_2$) or tungsten diselenide (WSe$_2$) inks can be used as the active layer of transistors[22] or photodetectors.[23] E2D inks report excellent chemical stability in ambient conditions,[24] tuneable p-type and n-type semiconductors,[25] and scalable production methods[26] paving the way to the next generation of solution processed electronics. Inkjet printed graphene FETs reached μ of up to 95 cm^2 V^{-1} s^{-1} and $I_{on}/I_{off} \approx 10$, on a surface-modified Si/SiO$_2$ substrate.[21] Fully inkjet-printed dielectrically-gated flexible graphene/h-BN FETs reported μ of up to 204 cm^2 V^{-1} s^{-1} on polyethylene terephthalate (PET) with $I_{on}/I_{off} \approx 2.5$ at low operating voltage (< 5 V) in ambient conditions.[10] These graphene/h-BN FETs enabled inkjet-printed ICs such as memories, logic gates, and CMOS with a gain of only $|A_v| \approx 0.1$.[10] Current modulation in printed thin films of LPE MoS$_2$, tungsten disulfide (WS$_2$), molybdenum diselenide (MoSe$_2$), and WSe$_2$ on PET has been attempted via electrochemical gating by a liquid electrolyte (LE), achieving $I_{on}/I_{off} \approx 600$ and $\mu \approx 0.1$ cm^2 V^{-1} s^{-1} for MoSe$_2$ and WS$_2$ films in vacuum.[22] However, the absence of printable highly crystalline semiconducting E2D inks able to exhibit field-effect modulation in ambient conditions has impeded the implementation of inkjet printed 2D material FETs suitable for digital ICs.[20,27]

Recently, improved solution-processing resulted in the production of high-quality semiconducting 2D materials by electrochemical intercalation of bulk MoS$_2$ layered crystals via quaternary ammonium molecules in acetonitrile.[28] Spin coated thin-films of the MoS$_2$ achieved μ of up to 10 cm^2 V^{-1} s^{-1} and $I_{on}/I_{off} \approx 10^6$ in vacuum with NMOS circuits with $|A_v| \approx 20$. However, the low concentration (<0.2 mg ml^{-1}) MoS$_2$ ink in dimethylformamide (DMF) makes them unsuitable for any scalable printing (such as inkjet). Inkjet printed CMOS logic has not yet been achieved with semiconducting E2D inks. In this work, we demonstrate circuits of CMOS and NMOS logic using inkjet printed n-type MoS$_2$ and p-type IDT-BT FETs achieving a mobility of up to 0.1 cm^2 V^{-1} s^{-1} at low voltage (<5 V) and fast switching times (as small as $\tau_{MoS2} \approx 3.5$ μs). The printed logics achieved $|A_v| \approx 4$ and $|A_v| \approx 1.4$ in NMOS and CMOS configurations, respectively.

2. Results and Discussion

2.1. Inks Formulation

We use inkjet printing as a versatile method to manufacture logic circuits. Ink properties such as surface tension γ, viscosity η, boiling point B_p, and concentration c must be engineered to ensure satellite droplet free ejection, high throughput, and morphologically uniform (i.e., roughness minimization) printed films.[7,10] The jetting of ink from an inkjet printer is determined by η, γ, density ρ, and the nozzle diameter, a.[29] The inverse of the Ohnesorge number (Oh) has been traditionally used as a figure of merit $Z = Oh^{-1} = (\gamma\rho a)^{1/2}/\eta$ to characterize the quality of droplet formation from the nozzle of an inkjet printer.[7] An optimal Z range to minimize the formation of satellite droplets (i.e., secondary droplets that are produced
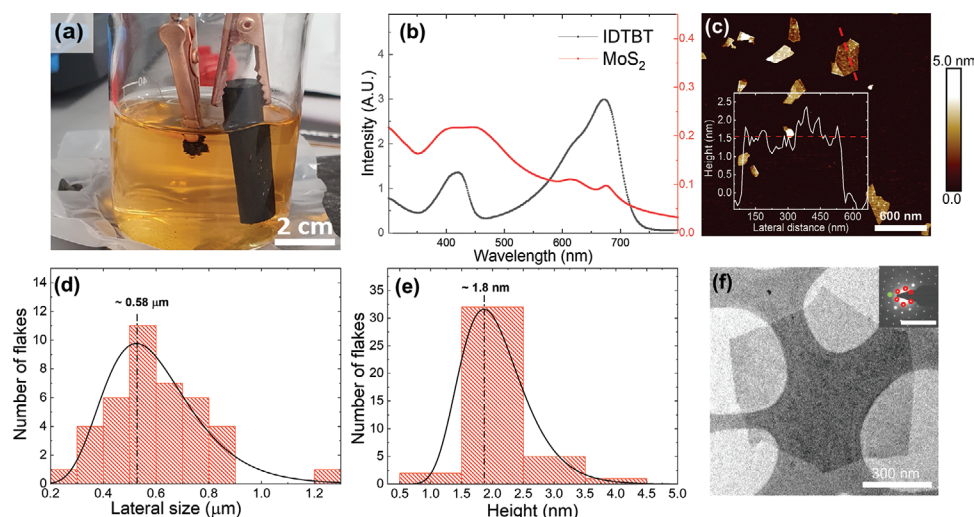
Figure 1. a) Electrochemical setup used to exfoliate a MoS$_2$ crystal. b) UV–Vis spectra of the MoS2 and IDT-BT. c) AFM micrograph of MoS$_2$ flakes with the scale indicating the maximum height being no more than 5 nm for the majority of flakes. The cross section of one of the MoS$_2$ flakes (red dashed line) is shown in the inset having a height of ≈1.5 nm. Lateral (d) and height (e) distribution of the MoS$_2$ flakes dispersed in IPA with the black curve showing the lognormal distribution of each dimension. f) TEM image of a MoS$_2$ flake along with the selective area diffraction pattern on the top right hand corner with the inset scale bar representing 10 nm. The diffraction pattern shows the (100) plane (red circles) and the (110) plane (green circle) which highlights the six-fold-symmetry.

in addition to the first droplet ejected from the inkjet nozzle)[29] from an inkjet nozzle has been identified as 2 < Z < 24. Therefore, we will engineer our ink to be within the optimal Z range to avoid any jetting issues. Inks with $c \approx 1$ mg ml^{-1} are required to maximize throughput while $\gamma \approx 30$ mN m^{-1} is optimal to coalesce the droplets after deposition. $B_p < 100$ °C ensures a quick evaporation of the solvent minimizing both the transport of particulates (which causes "coffee rings") and the re-dispersion of material after multiple passes, thus improving the morphological uniformity of the printed film.[10,30]

We intercalate the MoS$_2$ crystal with tetraheptylammonium (TA) cations to separate single and few-layer MoS$_2$ from the bulk crystal in acetonitrile/quaternary ammonium bromide electrolyte (**Figure 1**a).[28] The few-layer MoS$_2$ is then ultrasonicated in DMF with polyvinylpyrrolidone (PVP) (see Experimental Section). The MoS$_2$ is then solvent exchanged into isopropanol/PVP (IPA/PVP) by decanting the DMF and pipetting IPA/PVP into the sedimented MoS$_2$. We do this to engineer the inkjet printable n-type MoS$_2$ ink with $\eta_{MoS2} \approx 1.8$ mPa s, $\gamma_{MoS2} \approx 28$ mN m^{-1}, and $\rho_{MoS2} \approx 0.7$ g cm^{-3} (Figure S1, Supporting Information), consistent with our previous reports.[10,21] We select as a p-type ink the copolymer IDT-BT, synthesized according to the previously reported results[31] to use as a p-type material. We choose IDT-BT as it has previously demonstrated stability in air ambient for up to 100 h.[31] For printing the IDT-BT, we optimize the ink by dispersing at $c_{ID-TBT} \approx 6$ mg ml^{-1} in 1,2-dichlorobenzene (DCB) with $\eta_{ID-TBT} \approx 16$ mPa s, $\gamma_{IDTBT} \approx 20.6$ mN m^{-1}, and $\rho_{ID-TBT} \approx 1.3$ g cm^{-3} (Figure S1, Supporting Information). We find $Z \approx 11$ and $Z \approx 2$ for the MoS$_2$ and IDT-BT inks, respectively, which fall within the optimal printing range (Figure S2, Supporting Information).[10,21]

Figure 1b shows the UV–visible optical absorption spectra of the MoS$_2$ and IDT-BT inks. We use the Beer–Lambert law to correlate the absorbance (red line) to the c of MoS$_2$ flakes (see Experimental Section). We find $c \approx 2.65$ mg ml^{-1} for the MoS$_2$

ink (using an absorption coefficient $\alpha_{MoS2} \approx 3400$ L g^{-1} m^{-1}).[25] The spectra of the MoS$_2$ flakes displays two characteristic peaks at ≈ 610 and ≈ 672 nm attributed to the A exciton and B exciton, respectively, confirming the presence of MoS$_2$ flakes and consistent with the previous reports.[32] UV–vis spectroscopy also confirms the presence of IDT-BT, Figure 1b (black line) shows the characteristic peaks which are associated with the IDT-BT copolymer. The most prominent peak appears at ≈ 672 nm and is attributed the backbone of the C$_{16}$-IDT-BT polymer.[31,33]

The lateral size ($<L>$) and thickness (t) of the MoS$_2$ flakes is estimated using atomic force microscopy (AFM) statistics. An AFM micrograph of several MoS$_2$ flakes deposited on Si/SiO$_2$ substrate is shown in Figure 1c (also Figure S3, Supporting Information). The cross section of one of the MoS$_2$ flakes (red dashed line) is shown in the inset of Figure 1c with a thickness of 1.5 nm and lateral size of ≈ 550 nm. Figure 1d,e shows the log-normal distribution[34] of $<L>$ and t over 40 MoS$_2$ flakes. The t peaks at 1.8 nm (corresponding to an average number of layers, $N \approx 3$)[35] and $<L>$ peaks at 0.58 μm. A typical transmission electron microscopy (TEM) is shown in Figure 1f and a selected area electron diffraction image shown in the inset. The TEM agrees with the AFM data showing a lateral size of ≈ 1 μm while the diffraction pattern indicates the sixfold symmetry that is expected from MoS$_2$ flakes.[36,37] The MoS$_2$ $<L>$ determined from both TEM and AFM is about 2% the size of the nozzle diameter (21 μm), hence matching with the requirements of drop-on-demand (DOD) the inkjet printing.[21]

2.2. Inkjet Printed MoS$_2$ FETs

Before printing, we use electron-beam (e-beam) lithography to pattern ≈ 1 mm wide source, drain and gate electrodes on a Si/SiO$_2$ substrate (see Experimental Section). We use Ti/Au
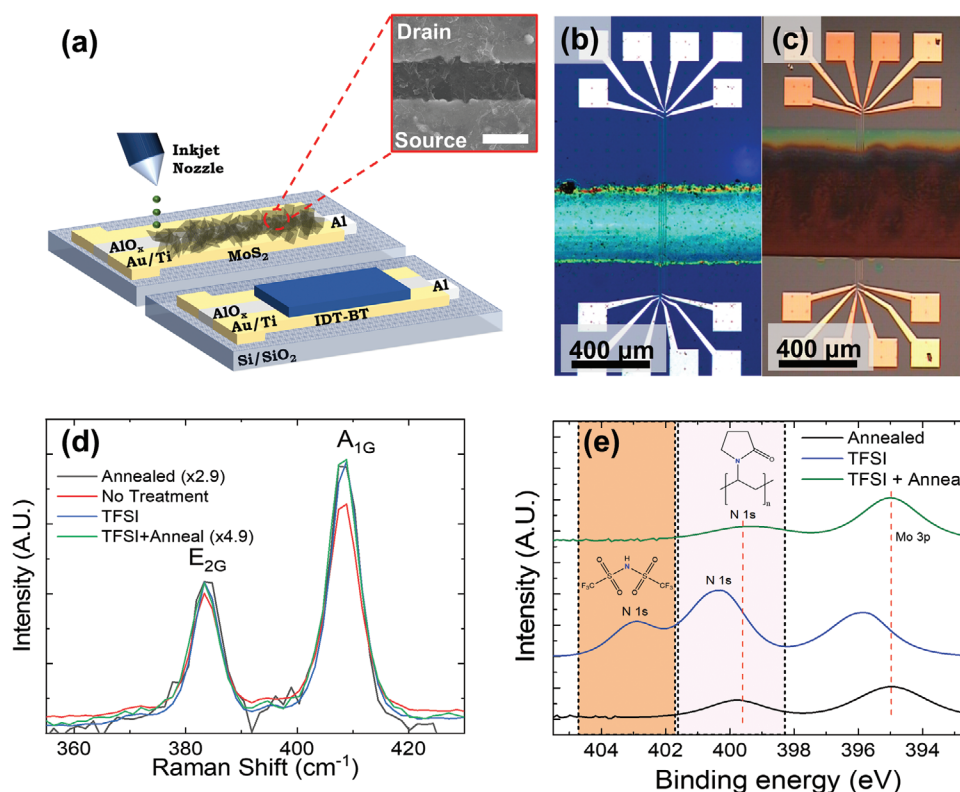
Figure 2. a) Schematic of the FETs with MOS$_2$ and IDT-BT inkjet printed channels across Ti/Au and Al/AlO$_x$ contacts. SEM image of the printed MoS$_2$ channel which shows MoS$_2$ flakes bridging the Ti/Au and Al/AlO$_x$ contacts, scale bar is 200 nm (inset). Optical microscope image of the b) MoS$_2$ and c) IDT-BT devices. d) Raman spectra of the inkjet printed MoS$_2$ channel at different treatment conditions, showing the characteristic E$_{2g}$ and A$_{1g}$ peaks. e) XPS spectra of MoS$_2$ flakes after TFSI + annealing (green), TFSI (blue), and annealed (cyan). A fitting was applied to the raw data (green, blue, and cyan curves) of each condition which is represented by the black curve. Each prominent peak was deconvoluted into its individual components, Mo 3p (red) and N 1s (pink). The MoS$_2$ flakes are responsible for the Mo 3p, whereas, N 1s is caused by the presence of PVP and TFSI as illustrated by the structural formula of these compounds.

(5/35 nm) for the source and drain and Al (40 nm) for gate electrodes of the FETs. A thin native AlO$_x$ layer (oxide thickness $t_{ox} \approx 4$ nm) is formed at the top surface of Al by air exposure, creating an Al/AlO$_x$ gate stack.[38] The gate length $L \approx 500$ nm, with the source-to-drain distance ≈ 100 nm longer.

We use a DOD inkjet printer to print the semiconductor channel and define the MoS$_2$ and IDT-BT FETs (**Figure 2**a) as follows. The MoS$_2$ ink is printed for 30 printing passes (i.e., where one pass is defined as an area with ink droplets deposited 30 µm from each other) over the source, drain, and gate electrodes to create the MoS$_2$ channel of the FET. We use an interdrop spacing (i.e., the center-to-center distance between two adjacent deposited droplets) of 30 µm with a platen temperature of 20 °C. We print with a channel width $W = 400$ µm. Profilometry measurements (see Experimental Section), reveal a channel thickness (t_c) as ≈ 20 nm, which matches the percolation threshold of inkjet printed E2D inks.[21] We use scanning electron microscopy (SEM) and AFM to confirm the MoS$_2$ flakes are covering the source, gate, and drain electrodes (Figure 2a, inset and Figure S4, Supporting Information). Further investigation with conductive AFM (see Experimental Section and Figure S5, Supporting Information) indicates that only a portion of the MoS$_2$ flakes (from 5.56% to 13.01% depending on the portion of channel scanned, on average $\approx 9.25\%$)

produce effective charge transport between the source and the drain electrodes, leading to an estimated effective $W \approx 40$ µm (see Figure S5, Supporting Information).

A post-processing treatment is required for the MoS$_2$ FETs to remove PVP stabilization agent after inkjet printing. We submerge our devices in bis(trifluoromethane)sulfonimide (TFSI) in 1,2-dichloroethane at 100 °C for 1 h. The treatment is performed in a nitrogen glovebox to avoid exposing TFSI to moisture in ambient atmosphere.[39] The devices are then annealed at 400 °C for 1 h to remove any residual solvent (see Experimental Section). Thermo-gravimetric analysis is undertaken on the PVP stabilization agent (see Experimental Section and Figure S7, Supporting Information) which indicates PVP starts to thermally decompose at ≈ 350 °C, with the rate of decomposition peaking at 434 °C indicating that the annealing step could also be assisting in the removal of PVP from the MoS$_2$ channel. We inkjet printed the IDT-BT ink at an interdrop spacing of 30 µm and platen temperature of 20 °C with 20 printing passes resulting in the same t_c (≈ 300 nm) as in the previous work.[31] The $W = 600$ µm for IDT-BT FETs. Optical microscopy is used to examine the inkjet printed MoS$_2$ (Figure 2b) and IDT-BT (Figure 2c) FETs. We observe that the films are printed over the source, drain, and gate electrodes as expected (Figure S6, Supporting Information).
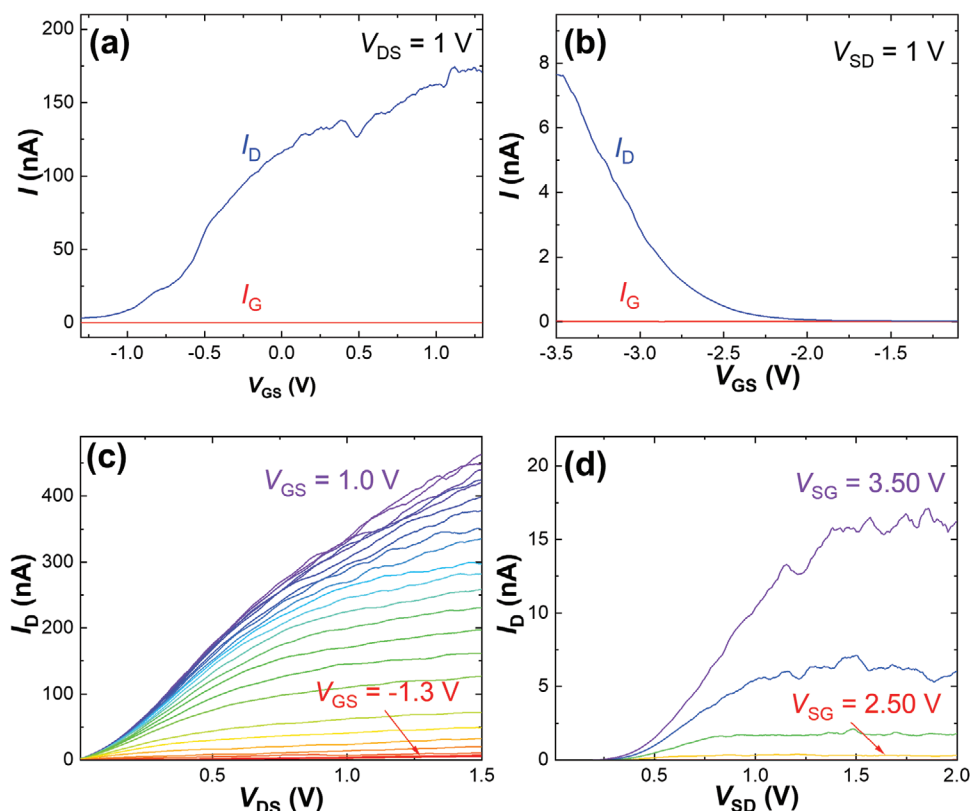
**ADVANCED
SCIENCE NEWS**
www.advancedsciencenews.com

**ADVANCED
ELECTRONIC
MATERIALS**
www.advelectronicmat.de

Figure 3. The transfer curve of the a) MoS$_2$ and b) IDT-BT FET which plots I_D as a function of V_{GS} with $|V_{DS}| = 1$ V. The gate current I_G is simultaneously measured (red curve). c) The output curves of the MoS$_2$ FET where the drain current I_D is measured as a function of V_{DS} (at V_{GS} ranging from −1.3 to 1 V with a step change of 0.1 V). d) The output curves of the IDT-BT FET with I_D measured as a function of V_{SD} (at V_{SG} ranging from 2.5 to 3.5 V with a step change of 0.25 V).

Raman spectroscopy is used to monitor the quality of the inkjet printed MoS$_2$ channel following the individual or combined effect of TFSI and annealing treatment. Figure 2d plots the spectra of the MoS$_2$ film as-deposited (red curve), after annealing and no TFSI treatment (black curve), after TFSI treatment and no annealing (blue curve) and after TFSI treatment followed by annealing (green curve). All spectra show the typical MoS$_2$ A$_{1g}$ and E$_{2g}$ peaks at 406 and 383 cm^{-1}, respectively.[40] The frequency difference (23 cm^{-1}) between A$_{1g}$ and E$_{2g}$ confirms an average thickness of few layers (3–4 layers).[41] The position of the E$_{2g}$ peak, Pos(E$_{2g}$) ≈ 383 cm^{-1}, indicates the absence of a large number of defects at every step of our post-processing treatment.[42]

X-ray photoelectron spectroscopy (XPS) is also used to determine the effect that TFSI treatment and annealing have on the MoS$_2$ inkjet printed films (Figure S8, Supporting Information). Figure 2e shows the XPS spectra of the MoS$_2$ ink in the energy region of 393 – 405 eV when TFSI treated (blue curve), annealed (cyan curve), and combined TFSI treatment followed by annealing (green line). The fits to the XPS curves are shown in black for the three cases. We select this region of the XPS spectra as it allows to us examine the respective changes in the binding energy of MoS$_2$ electrons for the three samples. The annealed MoS$_2$ sample (cyan curve) shows a peak at ≈ 395 eV, which corresponds to the Mo 3p peak and is associated with

molybdenum in MoS$_2$.[43] The position of the Mo 3p peak coincides in the TFSI treated and annealed MoS$_2$ sample (green curve), which upshifts to 396 eV in the TFSI treated MoS$_2$ samples (blue curve). We attribute this to the electronegative fluorine atom present in the molecular structure of TFSI. The fluorine atom attracts electron density towards itself from other surrounding atoms in molecules present in the thin film, hence, reducing the shielding of the nuclear charge and causing the binding energy of nearby atoms to increase.[44] Besides the Mo 3p peak, the three curves exhibit an N 1s orbital peak at ≈ 400 eV (pink curve) attributed to the nitrogen atom present in PVP[45] and another pink curve shows a second N 1s peak at ≈ 403 eV attributed to nitrogen atoms in TFSI.[46,47] Interestingly, while these peaks are quite intense in the blue curve, they are heavily suppressed in the green curve, indicating the removal of TFSI and a significant reduction of PVP concentration (with respect to the cyan curve), which also shows the same peak but significantly reduced. This indicates that the combination of TFSI and annealing treatments is necessary to minimize the presence of PVP which can otherwise degrade the electrical performance of our inkjet printed MoS$_2$ FET.

We characterize the electrical properties of the inkjet printed MoS$_2$ FETs and IDT-BT FETs using a probe station in air (see Experimental Section). For both FETs, the transfer characteristics (the drain current, I_D as a function of the gate-source
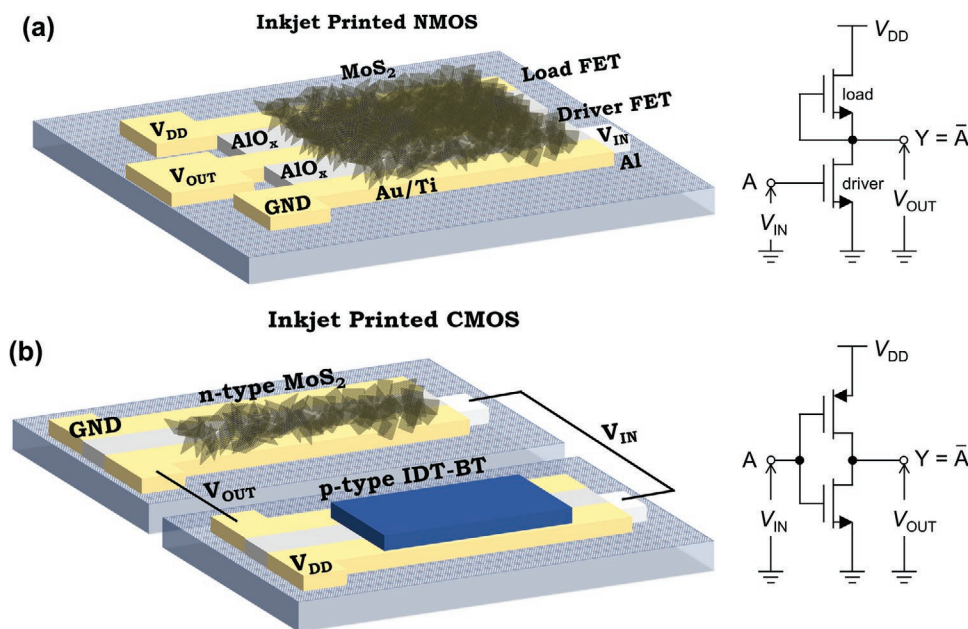
Figure 4. Schematic and circuit diagram of the inkjet printed a) NMOS and b) CMOS inverters.

voltage V_{GS}) (**Figure 3**a,b) are measured applying a drain-source voltage $|V_{DS}| = 1$ V (note that fluctuations in the curve are typical of all low-current devices). The MoS$_2$ FETs exhibit an n-type and IDT-BT FETs p-type behavior. The output characteristic (I_D as a function of the drain-source voltage, V_{DS}) of the MoS$_2$ FET (Figure 3c) is measured at V_{GS} ranging from −1.3 to 1.0 V with a step of 0.1 V. Conversely, the output curve of the IDT-BT FET (Figure 3d) is measured at V_{SG} ranging from 2.5 to 3.5 V with a step of 0.25 V. These curves are consistent with the behavior of MoS$_2$ FETs[28] and IDT-BT FETs[31] prepared by spin coating on Si/SiO$_2$ and glass substrates, respectively. The gate current in all the devices is $I_G < 100$ pA, which is three orders of magnitude smaller than the drain current (> 100 nA), indicating that the device is a modulating current in the semiconductor channel. Additionally, in the transfer curves (Figure 3a,b), the forward and backward sweep indicate minimal hysteresis (Figure S9, Supporting Information). The field-effect μ of the MoS$_2$ and IDT-BT FETs were derived from equation $\mu = (L/W) (1/C) (g_m/V_{DS})$, where $g_m = \partial I_D/\partial V_{GS}$ is the transconductance. We estimate the dielectric capacitance per unit area $C \approx 95$ nFcm^{-2} as an effective medium approximation of AlO$_x$ and air (Figure S10, Supporting Information) attributed to the variation of the peak to valley ($R_{pp} \approx 33$ nm) roughness of the gate for the MoS$_2$ FETs. We assume that the IDT-BT conforms to the gate roughness and is only gated by AlO$_x$ (Figure S6, Supporting Information). The ambient field-effect mobility for MoS$_2$ and IDT-BT FETs are calculated to be up to $\mu_{MoS2} \approx 0.06 \pm 0.02$ cm^2 V^{-1} s^{-1} and $\mu_{IDT-BT} \approx 2.7 \times 10^{-4} \pm 5 \times 10^{-5}$ cm^2 V^{-1} s^{-1}, with $I_{on}/I_{off} \approx$ 50 and 10^3 respectively. The best μ_{MoS2} was 0.1 cm^2 V^{-1} s^{-1} and $\mu_{IDT-BT} \approx 3.5 \times 10^{-4}$ cm^2 V^{-1} s^{-1}. The measured μ_{MoS2} is the extrinsic field effect mobility of the inkjet printed MoS$_2$ FET and we believe the value could be higher, if the contact resistance were to be reduced from a measured value of $R_c W \approx$ 656 MΩ μm. The μ is comparable to that of inkjet printed MoS$_2$

electrochemical transistors ($\mu \approx 0.1$ cm^2 V^{-1} s^{-1})[22] operating under high vacuum and lower than that of spin coated IDT-BT ($\mu \approx 1$ cm^2 V^{-1} s^{-1})[31] which we attribute to the higher roughness ($R_{pp} \approx 80$ nm) of the IDT-BT channel. We estimate the yield of working MoS$_2$ devices to be ≈ 50% for 24 devices and 100% for 26 IDT-BT devices.

The versatility of inkjet-printed n-type and p-type FETs allows us to easily design printed electronic circuits. Printed circuits with semiconducting E2D inks have been a long-sought milestone on the way towards the next generation of printed electronics. To verify the suitability of our technology to print circuits with 2D materials and the versatility to mutually operate with organic electronics, we demonstrate inkjet-printed NMOS and CMOS logic implementing the MoS$_2$ FETs in n-type MoS$_2$ depletion-load inverters (**Figure 4**a) and MoS$_2$/IDT-BT CMOS inverters (Figure 4b) shown in the schematic.

Figure 5a shows the static voltage transfer characteristic (the output voltage V_{OUT} as a function of the input voltage V_{IN}, blue line) and the corresponding low-frequency voltage gain $A_{v,NMOS}$ (red line, the scale on the right) of the NMOS inverter at the power supply voltage $V_{DD} = 1.5$ V. The device correctly operates as an inverter with a highest voltage gain $|A_{v,NMOS}| \approx 4$. Figure 5b shows the digital waveforms measured in the NMOS inverter. The input voltage swing is equal to V_{DD} (as in conventional logic gates) while the output voltage swing is ≈ 73% V_{DD}. The mismatch between V_{IN} and V_{OUT} logic voltage levels is attributed to the negative threshold voltage of the MoS$_2$ FETs.

The switching time (τ_{NMOS}), defined as the RC time constant of the output voltage in Figure 5b, is $\tau_{NMOS} \approx 400$ ms which is dominated by the large channel resistance (≈ 200 MΩ) and capacitive load of the BNC cables used to connect the FETs to the probe station. In contrast to FETs with liquid-electrolyte gates,[22] the fabricated gates are capable of operating at
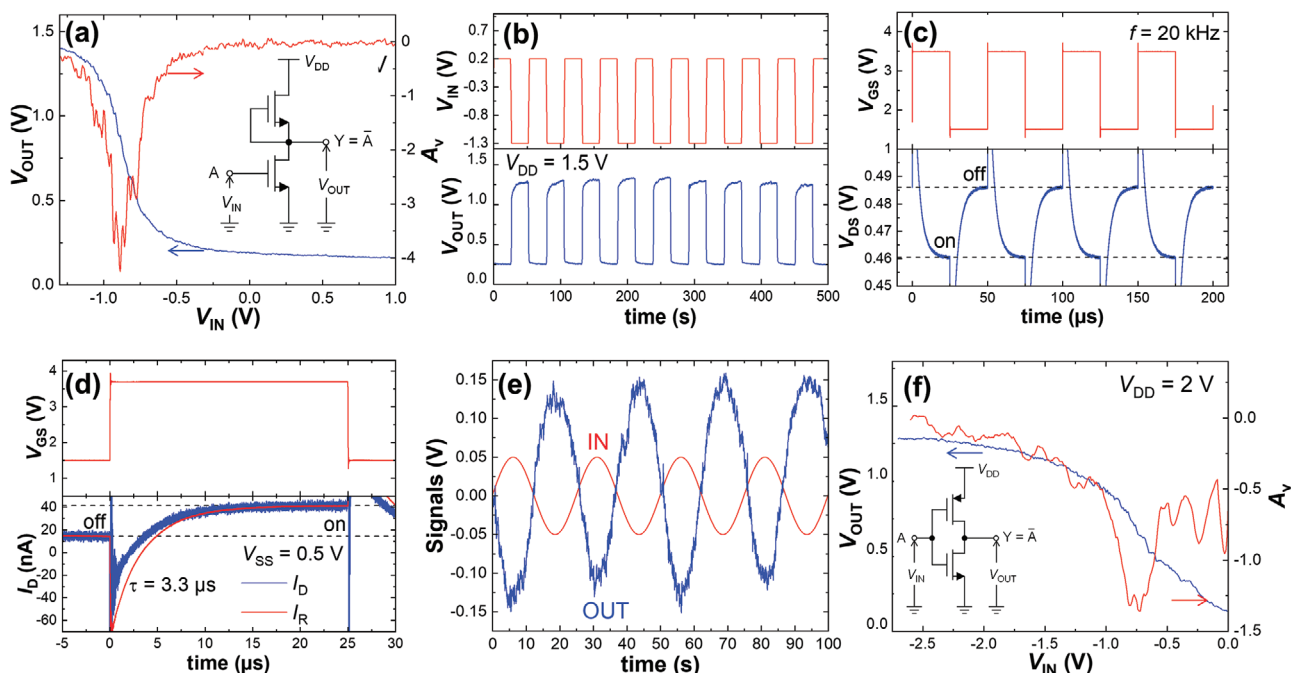
Figure 5. a) The static voltage transfer characteristic and the corresponding low-frequency frequency voltage gain (A_v) of an NMOS inverter. The circuit diagram shows the NMOS inverter made of a driver MoS$_2$ FET (bottom) and a load MoS$_2$ FET top. b) The digital V_{IN} (red) and V_{OUT} (blue) waveforms measured in the NMOS inverter as a function of time at V_{DD} = 1.5 V. c) The V_{DS} waveforms measured in the circuit comprising a single MoS$_2$ FET (see Figure S11, Supporting Information). V_{GS} is a square wave at 20 kHz. The spikes of V_{DS} are a consequence of the capacitive currents in the circuit. d) The same measurement in high temporal resolution reveals $\tau_{MoS2} \approx 3.3$ μs from the exponential decay fit. The plot shows both the drain current I_D and the resistive component of the drain current I_R (which is proportional to the drain potential). The difference between I_D and I_R is the capacitive component of the drain current I_C (Figure S11, Supporting Information) which approaches to zero in the steady state. e) The waveforms measured in the NMOS inverter operating as a small-signal voltage amplifier. The offsets are removed for clarity. f) The transfer characteristic of the fabricated CMOS inverter and the corresponding voltage gain at V_{DD} = 2 V.

high-frequency[48] and therefore do not significantly contribute to the time constant of the MoS$_2$ FETs. Figure 5c shows V_{DS} of an individual MoS$_2$ FET driven by a square wave V_{GS} at a frequency of 20 kHz (Figure S11, Supporting Information). The time constant of a single FET is mostly dominated by the drain time constant, that is, by the parasitic drain capacitances of the FET and drain load. This leads to an average time constant $\tau_{MoS2} \approx 4.1 \pm 0.4$ μs (Figure S12, Supporting Information) the much smaller compared to the NMOS inverter (due to the off-chip connections used to connect the FETs in the circuit) with the smallest τ_{MoS2} down to ≈ 3.3 μs (Figure 5d). The τ_{MoS2} here is smaller than that of the only printed MoS$_2$ transistors ($\tau \approx 68$ ms) reported on literature.[22] However, this is expected given the latter is an electrochemical transistor where the switching time is limited by the mass transfer of ions, unlike our FETs.

We also operate the inverter as a small-signal voltage amplifier as shown by the analogue waveforms measured in Figure 5e. The inverter is biased at the operating point where it exhibits the highest voltage gain (i.e., at $V_{IN} \approx -0.9$ V). The amplitude of the output voltage (blue curve) is ≈ 4 times larger than the amplitude of the input sine wave voltage (red curve), that is, $|A_{v,NMOS}| \approx 4$. We also realized CMOS inverters made of the inkjet printed IDT-BT p-type FETs and MoS$_2$ n-type FETs with a power supply voltage V_{DD} = 2 V. Figure 5f shows the transfer characteristics of the CMOS inverter and

the corresponding low-frequency voltage gain $A_{v,CMOS}$ of the CMOS inverter at the power supply voltages V_{DD} of 2 V. Also in this case the device correctly operates as an inverter, giving rise to $|A_v|_{CMOS} > 1$ at V_{DD} = 2 V. We find a maximum $A_{v,CMOS} \approx -1.4$ at V_{DD} = 2 V, which is higher than inkjet printed logic circuits previously reported with graphene inks, as expected.[10] However, the $|A_v|_{CMOS}$ is lower than our $|A_v|_{NMOS}$, which we attribute to a slight mismatch of V_{TH} and of I_D in the p-type and n-type FETs.

3. Conclusion

We demonstrated air-stable and low voltage (< 5 V) inkjet printed n-type MoS$_2$ with a fast switching time of $\tau_{MoS2} \approx 4.1 \pm 0.4$ μs, which is four orders of magnitude faster than state-of-the art solution processed MoS$_2$ transistors.[22] We integrated the MoS$_2$ FETs in NMOS logic and, with p-type IDT-BT FETs, in CMOS logic circuit architectures. The CMOS and NMOS inverters demonstrated a voltage gain of $|A_v|_{CMOS} \approx 1.4$ and $|A_v|_{NMOS} \approx 4$, respectively, which is ≈ 40 times greater than that of inkjet printed inverters with graphene inks.[10] The assembly of stable printed complementary logic combining 2D materials with organic polymers is a fundamental building block towards ubiquitous, low-cost, and high-performance digital electronics, which is manufacturable in a large scale.

**ADVANCED
SCIENCE NEWS**

www.advancedsciencenews.com

**ADVANCED
ELECTRONIC
MATERIALS**

www.advelectronicmat.de

4. Experimental Section

Electrochemical Exfoliation of MoS₂ and Ink Formulation: An electrochemical cell with two electrodes WAs used to intercalate a MoS_2 crystal (HQ graphene). Copper crocodile clips were used to mount the anode and cathode electrode. A thin piece of MoS_2 crystal was used as the cathode while a graphite rod (Qingdao Tennry Carbon Co.) was used as the anode. Tetraheptylammonium bromide (Sigma-Aldrich, CAS number: 4368-51-8, SKU: 87301) 5 mg ml⁻¹ was added to acetonitrile (≈ 50 ml) which acted as the electrolyte. The MoS_2 crystal and graphite rod should be completely submerged in the electrolyte. The authors applied a voltage of 8V and allowed the MoS_2 to be intercalated for 1 h. Further details on the reaction mechanism can be found in Lin et al.[28] After the reaction, the MoS_2 was intercalated with tetraheptylammonium cations and expanded increasing the volume of material on the crocodile clip. The MoS_2 was then washed with ethanol and manually broken into smaller pieces. The MoS_2 was then sonicated in DMF with PVP (Sigma-Aldrich, CAS Number 9003-39-8, SKU: PVP40) 22 mg ml⁻¹ (Molecular weight ≈ 40 000) for 30 min. To further assist the break-up of material, a shear mixer (IKA-T10) was then used for 10 min at 10 000 rpm. The dispersion was then centrifuged at 3000 rpm for 20 min (g ≈ 1534, r-max = 15.25 cm) to remove large chunks (> 10 layers) of MoS_2 material and then a further 5000 rpm for 10 min (g ≈ 4193, r-max = 15.25 cm). Both centrifuge steps made use of a ProteomeLab XL-A by Beckman Coulter coupled with an SW 32 Ti Swing-Bucket rotor. The resulting dispersion was a dark green color indicating the successful exfoliation of a few-layer MoS_2. Attempts to disperse the material directly in ethanol were not successful as the initial centrifugation step resulted in complete sedimentation. Therefore, the larger chunks could not be removed. The MoS_2/PVP/DMF dispersion was placed under high vacuum (operating at ≈1 mbar) at 40 °C for 240 min to concentrate 500 into 10 ml. The concentrated dispersion was then centrifuged at 45 000 rpm for 30 min (g ≈ 216 886, r-max = 9.58 cm) in a Beckman Optima MAX Ultracentrifuge to sediment the MoS_2. The MoS_2 sediment was then redispersed in IPA with PVP (22 mg ml⁻¹ (Molecular weight ≈40 000) to create the MoS_2 ink.

Formulation and Coating of IDT-BT: The hexadecyl alkyl side chain substituted IDT-BT was synthesized according to previously reported literature.[31] The IDT-BT polymer was dissolved in 1,2 dichlorobenzene at a c ≈ 6 mg ml⁻¹ for inkjet printing.

Fabrication of Electrodes and Dielectric on a Silicon Wafer: Highly doped Si chips with a thermally grown 90-nm-thick SiO_2 top layer were used in the fabrication of the MoS_2 FETs. The chips were initially cleaned by ultrasonication in acetone/isopropanol. The organic contamination from the surface of the chips was removed by O_2 plasma in a Tepla 300 AL PC plasma asher. Devices were patterned by e-beam lithography using a fixed-beam moving-stage (FBMS) mode of a Raith eLINE system at 30 keV. The FBMS mode allowed the authors to pattern very wide (950 μm) and very short (65 nm) electrodes without any stitching errors. Source and drain contacts (with a contact length of 1 μm and width W = 950 μm) were first defined by e-beam lithography followed by e-beam evaporation of Ti/Au (5/35 nm) in an e-beam evaporator at a base pressure of ≈ 1.2 × 10⁻⁶ mbar. Local back-gates (with a gate length L of 600 nm) were patterned by e-beam lithography in the second step followed by e-beam evaporation of Al (40 nm) in the e-beam evaporator at a base pressure of ≈ 1.2 × 10⁻⁶ mbar. A thin (≈ 4 nm) native AlO_x layer was formed at the top surface of Al after the samples were kept in air ambient for one day.

Inkjet Printing: A drop-on-demand inkjet printer (Fujifilm Dimatix DMP-2800) using a 21 μm diameter nozzle (Fujifilm DMC-11610) was used to print devices. For both MoS_2 and IDT-BT inks, one nozzle was used for printing with a droplet volume of ≈ 10 pL. An interdrop spacing of 30 μm with a platen temperature of 20 °C was used. Thirty printing passes (i.e., where one pass is defined as an area with ink droplets deposited 30 μm from each other) were used create the MoS_2 channels while twenty printing passes were used for the IDT-BT ink. The reduced number of printing passes was chosen so I_D in the on state matched in MoS_2 and IDT-BT FETs. Both inks were printed with a maximum jetting frequency of 2 kHz.

Film Treatment: The MoS_2 transistors were treated with 10 mg ml⁻¹ of TFSI (Sigma-Aldrich, CAS Number: 82113-65-3, SKU: 15220) in 1,2-dichloroethane (Acros Organics) at 100 °C for 1 h.[49] This was done in a nitrogen glovebox to minimize the exposure of TFSI to air. The film was then heated on a hot plate (in N_2 atmosphere) for 1 h at 400 °C.

Atomic Force Microscopy: A Bruker Dimension Icon working was used to analyze the area and thickness of the MoS_2 flakes contained in the E2D ink. The MoS_2 ink was drop cast onto a SiO_2 substrate after dilution by a factor of 1:100. The samples were scanned in peakforce mode, and 40 MoS_2 flakes were counted to determine the statistics for the lateral size and thickness. The lateral size was calculated as the square root of the flake length times the flake width. A NX-HighVac AFM working in tapping-contact mode (provided with a NCHR tip from NanoWorld) was used to analyze the surface roughness of the MoS_2 channel. The same apparatus was dotted with a solid Pt tip from Rocky Mountain (RMN-25PT300B) to collect current maps of the devices in contact mode, by applying a positive voltage to the AFM tip and keeping the drain electrode grounded.

Scanning Electron Microscopy: The SEM imaging was performed in Raith eLINE at 10 kV.

Profilometry: A Bruker DektakXT stylus profilometer was used to get the step height of the 30 layer printed films on Si/SiO₂ with a stylus tip radius of 12.5 μm and stylus force of 3 mg. The resolution of the profile was 0.666 μm/point and speed 200 μm s⁻¹. The data was obtained using Vision64.ink software.

Probe Station Measurement: All electrical measurements were performed in air ambient in FormFactor probe stations EP6 and Summit 11000. The electrical characterizations of the FETs and inverters were performed by Keithley 2600 series source-measure units at a typical sweep rate of 145 mV s⁻¹. The time constant was measured using a Tektronix AFG 3022B arbitrary function generator, Keysight DSO9404A digital storage oscilloscope (bandwidth 4 GHz), and Keysight N2795A active probe (bandwidth 1 GHz).

Raman Spectroscopy: Films of MoS_2 ≈ 200 nm thick were deposited onto Si/SiO₂ substrate, and a Raman spectrum was obtained using a Renishaw 1000 InVia micro-Raman spectrometer at 514.5 nm using a ×50 objective and incident power ≈1 mW.

Optical Absorption Spectroscopy: The flake concentration of the MoS_2 ink was found using the Beer–Lambert law which correlated the absorbance $A = \alpha c l$, to the flake concentration c, the absorption coefficient α, and the light path length l. The MoS_2 ink was diluted at a 1:200 ratio with DMF/PVP. An absorption coefficient of α_{MoS2} ≈ 3400 L g⁻¹ m⁻¹ for the MoS_2 ink at 660 nm was used.[25]

Surface Tension: The pendant drop method (First Ten Angstroms FTA1000B) was used to measure the MoS2 surface tension. Drop shape analysis was used to fit a shadow image of a droplet suspended from a needle and the surface tension was calculated using the Young–Laplace equation.[50]

Rheometry: A parallel plate rotational rheometer (DHR rheometer TA instruments) was used to calculate the infinite-rate viscosity of the MoS_2 ink. The measurement was taken at 25 °C.

Optical Microscope: An optical microscope (Nikon Optiphot 300 attached to Schott ACE 1 light source) was used to image deposited droplets in dark field mode. The images were acquired at a ×20 magnification.

Transmission Electron Microscopy: The TEM was performed with a FEI Philips Tecnai F-20 operated at 200 kV (Tungsten, LB6) with a line resolution of 0.10 and point resolution of 0.24 nm. Spherical aberration Cs (objective): 1.2 mm. The IPA/PVP-MoS_2 ink was diluted by a factor of 100 and drop cast on holey carbon film 400 mesh copper (Cu) grid (Agar scientific product code AGS147-4) and allowed to dry naturally overnight.

X-Ray Photoelectron Spectroscopy: K-Alpha+ surface analysis by Thermo scientific was used to obtain the XPS data of the MoS_2 films. The spectra were obtained under 8 × 10⁻⁷ mbar (ultra-vacuum) which employed micro-focused Al Kα X-ray source (1486 eV) and a 2D detector attached to a 180 double-focusing hemispherical analyzer. The data obtained were further analyzed using Avantage software by Thermo scientific.

Thermogravimetric Analysis: TGA measurements of the PVP were performed with a TA Instruments Q50 under nitrogen with a ramping temperature of 10 °C min^{-1} from ≈ 25 up to 1000 °C.

Supporting Information

Supporting Information is available from the Wiley Online Library or from the author.

Conflict of Interest

The authors declare no conflict of interest.

Data Availability Statement

The data supporting this paper are available at https://data.hpc.imperial.ac.uk/.

[1] S. Voinigescu, *High-Frequency Integrated Circuits*, Cambridge University Press, Cambridge **2013**.

[2] J. P. Uyemura, *CMOS Logic Circuit Design*, Springer, Boston **2002**.

[3] J. P. Uyemura, *Circuit Design for CMOS VLSI*, Springer, Boston, MA **1992**.

[4] R. J. Baker, *CMOS: Circuit Design, Layout, and Simulation: Third Edition*, **2011**.

[5] X. Cao, C. Lau, Y. Liu, F. Wu, H. Gui, Q. Liu, Y. Ma, H. Wan, M. R. Amer, C. Zhou, *ACS Nano* **2016**, *11*, 9816.

[6] A. Nathan, A. Ahnood, M. T. Cole, S. Lee, Y. Suzuki, P. Hiralal, F. Bonaccorso, T. Hasan, L. Garcia-Gancedo, A. Dyadyusha, S. Haque, P. Andrew, S. Hofmann, J. Moultrie, D. Chu, A. J. Flewitt, A. C. Ferrari, M. J. Kelly, J. Robertson, G. A. J. Amaratunga, W. I. Milne, *Proc. IEEE* **2012**, *100*, 1486.

[7] F. Torrisi, T. Carey, *Nano Today* **2018**, *23*, 73.

[8] C. Liu, H. Chen, S. Wang, Q. Liu, Y. G. Jiang, D. W. Zhang, M. Liu, P. Zhou, *Nat. Nanotechnol.* **2020**, *15*, 545.

[9] T. Shimoda, Y. Matsuki, M. Furusawa, T. Aoki, I. Yudasaka, H. Tanaka, H. Iwasawa, D. Wang, M. Miyasaka, Y. Takeuchi, *Nature* **2006**, *440*, 783.

[10] T. Carey, S. Cacovich, G. Divitini, J. Ren, A. Mansouri, J. M. Kim, C. Wang, C. Ducati, R. Sordan, F. Torrisi, *Nat. Commun.* **2017**, *8*, 1202.

[11] A. J. Cho, K. C. Park, J. Y. Kwon, *Nanoscale Res. Lett.* **2015**, *10*, 115.

[12] G. E. Moore, *Proc. IEEE* **1998**, *86*, 82.

[13] D. Akinwande, C. Huyghebaert, C. H. Wang, M. I. Serna, S. Goossens, L. J. Li, H. S. P. Wong, F. H. L. Koppens, *Nature* **2019**, *573*, 507.

[14] M. Singh, H. M. Haverinen, P. Dhagat, G. E. Jabbour, *Adv. Mater.* **2010**, *22*, 673.

[15] H. Yan, Z. Chen, Y. Zheng, C. Newman, J. R. Quinn, F. Dötz, M. Kastler, A. Facchetti, *Nature* **2009**, *457*, 679.

[16] H. Wang, P. Wei, Y. Li, J. Han, H. R. Lee, B. D. Naab, N. Liu, C. Wang, E. Adijanto, B. C. K. Tee, S. Morishita, Q. Li, Y. Gao, Y. Cui, Z. Bao, *Proc. Natl. Acad. Sci. USA* **2014**, *111*, 4776.

[17] B. Kim, S. Jang, M. L. Geier, P. L. Prabhumirashi, M. C. Hersam, A. Dodabalapur, *Nano Lett.* **2014**, *14*, 3683.

[18] T. Hodsden, K. J. Thorley, J. Panidi, A. Basu, A. V. Marsh, H. Dai, A. J. P. White, C. Wang, W. Mitchell, F. Glöcklhofer, T. D. Anthopoulos, M. Heeney, *Adv. Funct. Mater.* **2020**, *30*, 2000325.

[19] A. F. Paterson, S. Singh, K. J. Fallon, T. Hodsden, Y. Han, B. C. Schroeder, H. Bronstein, M. Heeney, I. McCulloch, T. D. Anthopoulos, *Adv. Mater.* **2018**, *30*, 1801079.

[20] F. Torrisi, J. N. Coleman, *Nat. Nanotechnol.* **2014**, *9*, 738.

[21] F. Torrisi, T. Hasan, W. Wu, Z. Sun, A. Lombardo, T. S. Kulmala, G. W. Hsieh, S. Jung, F. Bonaccorso, P. J. Paul, D. Chu, A. C. Ferrari, *ACS Nano* **2012**, *6*, 2992.

[22] A. G. Kelly, T. Hallam, C. Backes, A. Harvey, A. S. Esmaeily, I. Godwin, J. Coelho, V. Nicolosi, J. Lauth, A. Kulkarni, S. Kinge, L. D. A. Siebbeles, G. S. Duesberg, J. N. Coleman, *Science* **2017**, *356*, 69.

[23] D. J. Finn, M. Lotya, G. Cunningham, R. J. Smith, D. McCloskey, J. F. Donegan, J. N. Coleman, *J. Mater. Chem. C* **2014**, *2*, 925.

[24] X. Wang, Y. Sun, K. Liu, *2D Mater.* **2019**, *6*, 042001.

[25] J. N. Coleman, M. Lotya, A. O'Neill, S. D. Bergin, P. J. King, U. Khan, K. Young, A. Gaucher, S. De, R. J. Smith, I. V. Shvets, S. K. Arora, G. Stanton, H. Y. Kim, K. Lee, G. T. Kim, G. S. Duesberg, T. Hallam, J. J. Boland, J. J. Wang, J. F. Donegan, J. C. Grunlan, G. Moriarty, A. Shmeliov, R. J. Nicholls, J. M. Perkins, E. M. Grieveson, K. Theuwissen, D. W. McComb, P. D. Nellist, V. Nicolosi, *Science* **2011**, *331*, 568.

[26] K. R. Paton, E. Varrla, C. Backes, R. J. Smith, U. Khan, A. O'Neill, C. Boland, M. Lotya, O. M. Istrate, P. King, T. Higgins, S. Barwich, P. May, P. Puczkarski, I. Ahmed, M. Moebius, H. Pettersson, E. Long, J. Coelho, S. E. O'Brien, E. K. McGuire, B. M. Sanchez, G. S. Duesberg, N. McEvoy, T. J. Pennycook, C. Downing, A. Crossley, V. Nicolosi, J. N. Coleman, *Nat. Mater.* **2014**, *13*, 624.

[27] D. Akinwande, *Nat. Nanotechnol.* **2017**, *12*, 287.

[28] Z. Lin, Y. Liu, U. Halim, M. Ding, Y. Liu, Y. Wang, C. Jia, P. Chen, X. Duan, C. Wang, F. Song, M. Li, C. Wan, Y. Huang, X. Duan, *Nature* **2018**, *562*, 254.

[29] J. E. Fromm, *IBM J. Res. Dev.* **1984**, *28*, 322.

[30] T. Carey, C. Jones, F. L. Moal, D. Deganello, F. Torrisi, *ACS Appl. Mater. Interfaces* **2018**, *10*, 19948.

[31] W. Zhang, J. Smith, S. E. Watkins, R. Gysel, M. McGehee, A. Salleo, J. Kirkpatrick, S. Ashraf, T. Anthopoulos, M. Heeney, I. McCulloch, *J. Am. Chem. Soc.* **2010**, *132*, 11437.

[32] J. Li, M. M. Naiini, S. Vaziri, M. C. Lemme, M. Östling, *Adv. Funct. Mater.* **2014**, *24*, 6524.

[33] C. R. Snyder, D. M. DeLongchamp, *Curr. Opin. Solid State Mater. Sci.* **2018**, *22*, 41.

[34] K. Kouroupis-Agalou, A. Liscio, E. Treossi, L. Ortolani, V. Morandi, N. M. Pugno, V. Palermo, *Nanoscale* **2014**, *6*, 5926.

[35] K. D. Rasamani, F. Alimohammadi, Y. Sun, *Mater. Today* **2017**, *20*, 83.

[36] Z. Guo, W. Cui, X. Zheng, W. Liu, X. Tong, Q. Xu, *Surf. Interfaces* **2018**, *12*, 41.

[37] Y. Li, Y. Rao, K. F. Mak, Y. You, S. Wang, C. R. Dean, T. F. Heinz, *Nano Lett.* **2013**, *13*, 3329.

[38] E. Guerriero, L. Polloni, M. Bianchi, A. Behnam, E. Carrion, L. G. Rizzi, E. Pop, R. Sordan, *ACS Nano* **2013**, *7*, 5588.

[39] M. Vilkman, A. Lankinen, N. Volk, P. Kostamo, O. Ikkala, *Polymer* **2010**, *51*, 4095.

[40] H. Li, Q. Zhang, C. C. R. Yap, B. K. Tay, T. H. T. Edwin, A. Olivier, D. Baillargeat, *Adv. Funct. Mater.* **2012**, *22*, 1385.

[41] C. Lee, H. Yan, L. E. Brus, T. F. Heinz, J. Hone, S. Ryu, *ACS Nano* **2010**, *4*, 2695.

[42] W. M. Parkin, A. Balan, L. Liang, P. M. Das, M. Lamparski, C. H. Naylor, J. A. Rodríguez-Manzo, A. T. C. Johnson, V. Meunier, M. Drndić, *ACS Nano* **2016**, *10*, 4134.

[43] Y. Wu, P. Jiang, M. Jiang, T. W. Wang, C. F. Guo, S. S. Xie, Z. L. Wang, *Nanotechnology* **2009**, *20*, 305602.

[44] J. F. Watts, J. Wolstenholme, *An Introduction to Surface Analysis by XPS and AES*, Wiley & Sons, Chichester **2003**.

[45] S. Caporali, U. Bardi, A. Lavacchi, *J. Electron Spectrosc. Relat. Phenom.* **2006**, *151*, 4.

[46] S. Tardio, P. J. Cumpson, *Surf. Interface Anal.* **2018**, *50*, 5.

[47] G. Greczynski, L. Hultman, *Prog. Mater. Sci.* **2020**, 107.

[48] E. Guerriero, P. Pedrinazzi, A. Mansouri, O. Habibpour, M. Winters, N. Rorsman, A. Behnam, E. A. Carrion, A. Pesquera, A. Centeno, A. Zurutuza, E. Pop, H. Zirath, R. Sordan, *Sci. Rep.* **2017**, *7*, 2419.

[49] M. Amani, D. H. Lien, D. Kiriya, J. Xiao, A. Azcatl, J. Noh, S. R. Madhvapathy, R. Addou, K. C. Santosh, M. Dubey, K. Cho, R. M. Wallace, S. C. Lee, J. H. He, J. W. Ager, X. Zhang, E. Yablonovitch, A. Javey, *Science* **2015**, *350*, 1065.

[50] Y. Yuan, T. R. Lee, in *Surface Science Techniques. Springer Series in Surface Sciences* (Eds: G. Bracco, B. Holst), Vol. 51, Springer, Berlin, Heidelberg **2013**.